Nano Research

Open Access

Research Article

Fe single atom-doped on canola meal-derived carbon for efficient oxygen reduction reaction

Jianping Guan[1,§], Chenyang Huang[1,§], Donghao Liu[1], Bao Li[2], Tonghua Wang[2], Jiaxin Gong[1], Xu Liu[1], Huanran Zheng[1], and Yu Xiong[1,2] ✉

[1] College of Chemistry and Chemical Engineering, Central South University, Changsha 410083, China
[2] Yuelushan Laboratory, Changsha 410082, China
[§] Jianping Guan and Chenyang Huang contributed equally to this work.

Cite this article: *Nano Research*, **2026**, *19*, 94908051. https://doi.org/10.26599/NR.2025.94908051

ABSTRACT: Pursuing both high catalytic performance and low cost is the key to developing applicable electrocatalysts for oxygen reduction reaction (ORR). In this work, we developed Fe single atom-doped on sulfur and nitrogen co-doped carbon catalysts (Fe_1/SCN-cm) using canola (*Brassica napus L.*) meal as the precursors, which show high catalytic performance in ORR with the half-wave potential as high as 0.92 V. Notably, Fe_1/SCN-cm also presents a high stability with only a 13 mV decrease after 10,000 cycle tests. The sulfur directly derived from canola (*Brassica napus L.*) meal and the porous structure with high surface area are the key to the high catalytic performance of Fe_1/SCN-cm. It is believed that this work provides a new arsenal for the synthesis of metal single atom catalysts and directions for the valorisation of canola meal.

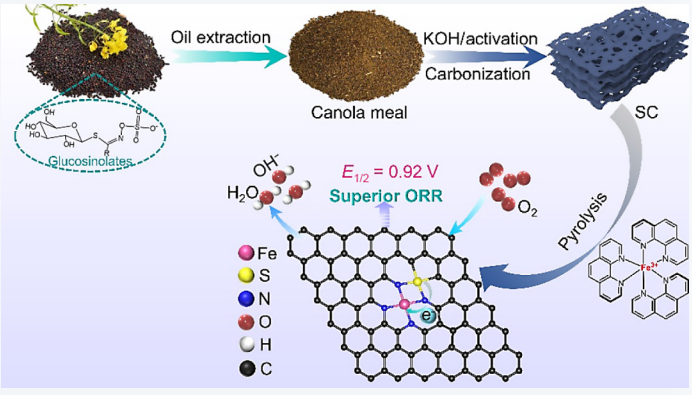

KEYWORDS: single atom catalyst, canola meal, sulfur doping, oxygen reduction reaction

1 Introduction

Single atom catalysts (SACs) have attracted much attention in last decades [1–5], since their ultra-high atom efficiency as well as unexpected catalytic performance [6–10]. Fe single atom-doped on nitrogen-doped carbon catalysts (Fe_1/CN) with Fe–N_x active moiety are found to be highly efficient in oxygen reduction reaction (ORR) [11–15], which are regarded as potential catalysts to replace nanosized Pt catalysts for future energy conversion and storage [16–18]. The dopant of heteroatoms, including P [19, 20], S [21–23], and B [24–27], can alter the electronic structure of Fe and thus improve the ORR activity of Fe_1/CN [28]. For example, Zhao et al. reported that sulphur directly bonded with iron adjusts the electronic structure of Fe and thus exhibits high ORR activity with a halfwave potential of 0.93 V [29]. Yu et al. reported that the long-range interaction between S and Fe induces much higher ORR catalytic activity than the direct coordination [30]. However, the complicated synthetic procedure as well as the high price of the precursors reduce their economic viability of heteroatom-doped Fe_1/CN. Therefore, simultaneously synthesizing heteroatom-doped Fe_1/CN from both catalytic activity and economic sides is of great importance.

Canola (*Brassica napus L.*) is the second-largest cultivated oilseed crop in the world, with 85.24 million tons supplied (a 12.60% share of total production) [31]. Though containing high quality of proteins with a protein digestibility corrected amino acids score as high as 0.81, the high content of anti-nutritional factors in canola meal, including thioglycosides, fiber, phytic acid, and sinapine, limits their application in animal farming and aquaculture, with only 0.14% of the global plant-based protein market [32–34]. Though containing the similar high content of fiber as coconut shell, the high content of S hinders the conversion of canola meal to activated carbon [35]. On the other hand, the high content of fiber can be a good foundation in graphitic support, and the S content derived from canola meal may be a natural S source to enhance the catalytic performance of Fe_1/CN [36]. Therefore, it may be a good chance to develop the synthetic strategy for Fe_1/CN derived from canola meal [37, 38].

Received: July 21, 2025; **Revised:** September 1, 2025
Accepted: September 8, 2025

✉Address correspondence to thomas153@126.com

In this work, S-doped Fe_1/CN were fabricated via a coordinated impregnation strategy, where S-doped carbon support was directly derived from canola meal (Fe_1/SCN-cm). Fe_1/SCN-cm shows the high catalytic performance in ORR with a high half-wave potential of 0.92 V, which is higher than most of reported Fe_1/CN as far as we know [39–44]. Moreover, the as synthesized Fe_1/SCN-cm also exhibits a good stability with only 13 mV decrease after 10,000 cycles. The high surface area and the dopant of S are ascribed to be the main reason for the high catalytic performance. More importantly, Fe_1/SCN-cm is used as the component of air cathode in zinc air batteries (ZABs), showing more than 320 h stable operation in the galvanostatic cycling stability tests. This work provides a potential approach to convert canola meal to SACs.

2 Results and discussion

The schematic illustration is shown in Fig. 1(a). The canola meal used in this study was obtained from rapeseed after extracting oil. From scanning electron microscopy (SEM) and transmission electron microscopy (TEM) images, canola meal shows a layered structure with numerous pores, indicating the high potential for converting into graphitic catalysts with high surface area (Fig. S1 in the Electronic Supplementary Material (ESM)). Canola meal was first pre-carbonized at 500 °C for 1 h. During this process, nitrogen species decomposed and evaporated with the volatile substance, including the remaining oil. After pyrolyzing with KOH at 900 °C for 3 h under N_2 atmosphere, the sulfur-doped biocarbon support (SC) was obtained. From SEM and TEM images, SC maintained

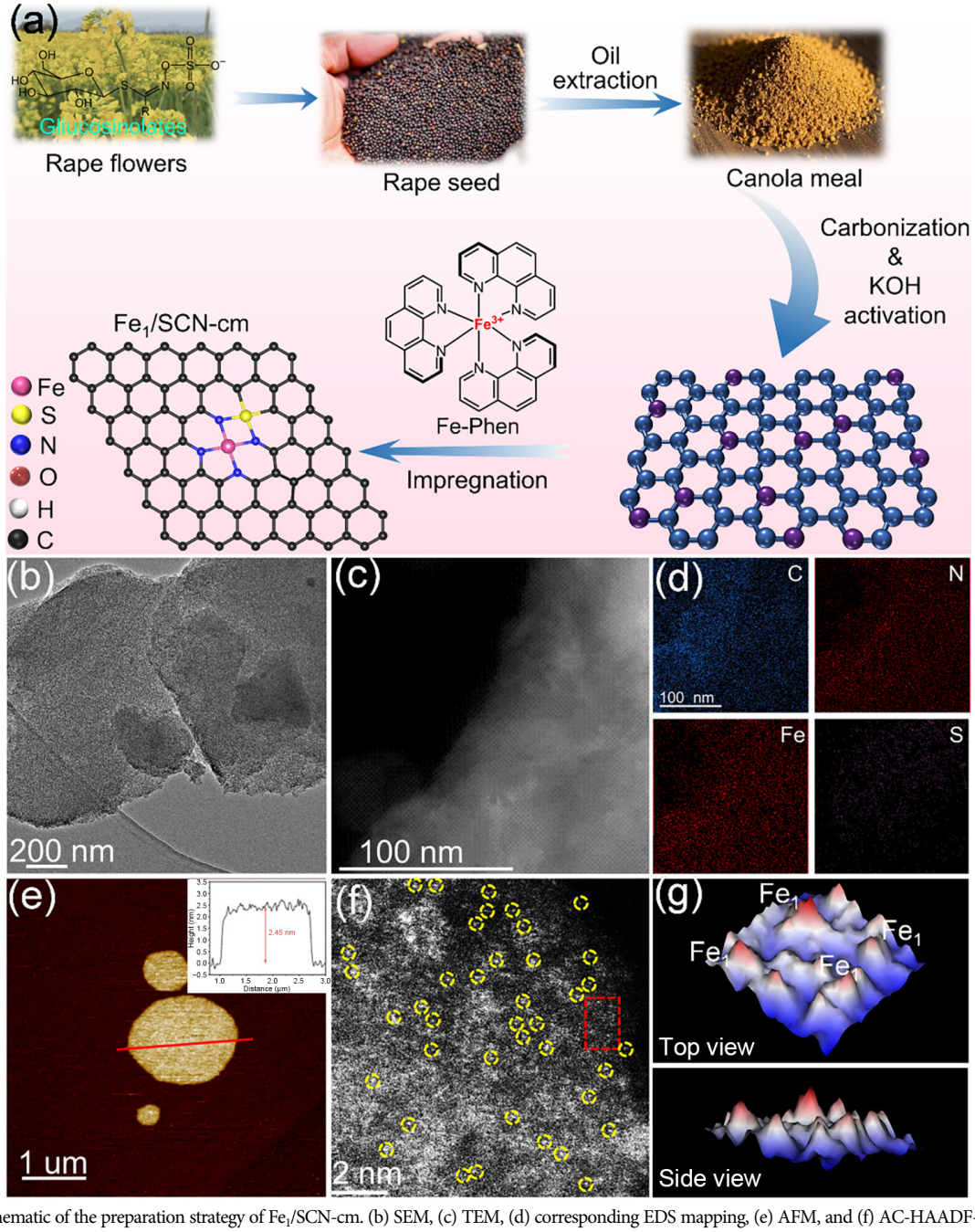

Figure 1 (a) Schematic of the preparation strategy of Fe_1/SCN-cm. (b) SEM, (c) TEM, (d) corresponding EDS mapping, (e) AFM, and (f) AC-HAADF-STEM images of Fe_1/SCN-cm. (g) The images of 3D Fe atom sites, overlapping Gaussian-function fitting mappings of the area marked by a red square in (f).

the initial layered structure with micropores, which is attributed to the intercalation of molten K^+ (Fig. S2 in the ESM). After the impregnation of Fe precursors and 1,10-phenanthroline on SC and pyrolysis at 900 °C under N_2 atmosphere, Fe_1/SCN-cm was obtained. Notably, no other sulfur sources are added in the synthetic process, and all the sulfur is directly derived from canola meal.

Powder X-ray diffraction (PXRD) patterns show peaks located at 23.5° and 45.7°, which can be ascribed to the (200) and (101) facets of graphite (Fig. S3 in the ESM). SEM and TEM images show that Fe_1/SCN-cm maintained the layered structure with micropores (Figs. 1(b) and 1(c)). The results from scanning TEM image and its corresponding energy dispersion spectroscope (EDS) mapping indicate that C, N, S, and Fe are homogeneously distributed on the support (Fig. 1(d)). Atomic force microscopy (AFM) image and the corresponding height analysis are shown in Fig. 1(e), from which we can see the thickness of Fe_1/SCN-cm is 2.48 nm. The high atomic-number (Z) contrast gives us an opportunity to certify Fe atoms from light elements (C, N, and O) in aberration-corrected high-angle annular dark-field scanning TEM (AC-HAADF-STEM) image, and Fe single atoms are marked by yellow cycles in Fig. 1(f). Moreover, the three-dimensional (3D) atomic overlap Gaussian function fitting analysis diagram of the red-marked region in Fig. 1(g) further confirms the presence of numerous atomically dispersed Fe sites in the carbon support.

The nitrogen adsorption–desorption isotherms and corresponding pore size distribution analysis revealed the surface or porous structure of SC and Fe_1/SCN-cm materials with varying dosages of Fe precursors (Fe_1/SCN-cm-x, where x represents the dosage of Fe precursors) (Figs. S4 and S5 and Table S1 in the ESM). Their adsorption–desorption isotherms exhibit a sharp increase in adsorption capacity at low relative pressures (strong adsorption potential for microspores), capillary condensation in the medium-pressure region with hysteresis loops, and a gradual flattening at high pressures, which is consistent with the characteristics of Types I and IV isotherm curves. The ultra-high Brunauer–Emmett–Teller (BET) specific surface areas of Fe_1/SCN-cm-2 (2913.4 $m^2 \cdot g^{-1}$), Fe_1/SCN-cm-4 (2846.7 $m^2 \cdot g^{-1}$), Fe_1/SCN-cm (2346.6 $m^2 \cdot g^{-1}$), Fe_1/SCN-cm-8 (2264.2 $m^2 \cdot g^{-1}$), Fe_1/SCN-cm-10 (1996.0 $m^2 \cdot g^{-1}$), and SC (2672.5 $m^2 \cdot g^{-1}$) indicate that the insertion of molten K^+ enlarges the pore and thus increase the surface area. Notably, the specific surface area of the catalysts decreased progressively with the increase in the dosage of Fe, verifying that the addition of Fe can occupy the defect of the support, which decreases the surface area of catalysts. Additionally, the pore size distribution curves demonstrate that both Fe_1/SCN-cm and SC contain abundant micropores, with pore sizes ranging from 2.53 to 2.90 nm. These results suggest that Fe_1/SCN-cm is a microporous material, whose ultrahigh specific surface area and abundant microporous structure facilitate the exposure of catalytic active sites and enhance mass transfer, thereby boosting its catalytic performance. Moreover, the D band and G band signals with Raman shift of 1297.8 and 1573.9 cm^{-1}, respectively are observed in Raman spectrum with intensity ratio of the D and G bands (I_D/I_G) = 1.33, certifying the defect-rich graphitic nature of Fe_1/SCN-cm (Fig. S6 in the ESM). Element analysis (EA) results indicate that the sulfur content was maintained, while nitrogen decomposed and evaporated during synthesis, suggesting that the sulfur in Fe_1/SCN-cm is derived from canola meal, and the addition of 1,10-phenanthroline mainly contributed to nitrogen content (Table S2 in the ESM). From the result of inductively coupled plasma optical emission spectra (ICP-OES), 0.706% Fe loading was detected in Fe_1/SCN-cm.

X-ray photoelectron spectroscopy (XPS) was carried out to certify the chemical state of C, N, and S in Fe_1/SCN-cm with SC and canola meal as reference samples. From XPS survey spectrum, we can see that C, N, and S are the major components in Fe_1/SCN-cm (Fig. S7 in the ESM). Additionally, N signals cannot be seen in the spectrum of SC, since nitrogen from protein or nucleic acid decomposes during high temperature (Fig. S8 in the ESM). C 1s XPS spectra of these samples can be deconvoluted into three peaks, which are assigned to C=C (284.8 eV), C–N/O (285.7 eV), and C=O (289.2 eV; Fig. 2(a) and Fig. S9 in the ESM) [36, 37]. Notably, the content of C–N/O decreases obviously in C 1s spectrum of SC, further indicating the decomposition of nitrogen. Moreover, N 1s spectrum of Fe_1/SCN-cm show three main peaks situated at graphitic-N (402.2 eV), pyrrolic-N (400.2 eV), and pyridinic-N (398.4 eV) [38], respectively, indicating that the nitrogen from 1,10-phenanthroline partially coordinated with Fe and converted into graphitic-N (Fig. 2(b) and Fig. S10 in the ESM). In addition, due to the extremely low Fe content in Fe_1/SCN-cm, no obvious peaks were detected in the Fe 2p spectrum of Fe_1/SCN-cm (Fig. S11 in the ESM) [40, 41]. The two main peaks situated at $2p_{3/2}$ and $2p_{1/2}$ branches of C–SO_x–C species (168.7 and 169.8 eV), and two minor peaks situated at the $2p_{3/2}$ and $2p_{1/2}$ branches of C–S–C species (163.3 and 164.4 eV) are detected in S 2p XPS spectra of Fe_1/SCN-cm and reference samples [45, 46]. Though S species are directly derived from canola meal, the content of different S species is altered during the synthetic process (Fig. 2(c) and Fig. S12 in the ESM).

In order to further certify the microstructure of Fe_1/SCN-cm, extended X-ray absorption fine structure (EXAFS) spectra were performed. The energy of the absorption peak of Fe_1/SCN-cm near that of Fe_3O_4 in X-ray absorption near-edge structure (XANES), indicating a +2–+3 chemical state of Fe (Figs. 2(d) and 2(e)). Moreover, the chemical state analysis of the energy of the absorption peak further certifies that the chemical state of Fe single atoms in Fe_1/SCN-cm is 2.93 (Fig. S13 in the ESM). No detectable Fe–Fe bonds (approximately 2.2 Å) and obvious signal at 1.4 Å, attributed to Fe–N bond, can be observed in Fourier-transformed EXAFS (FT-EXAFS) spectra (Fig. 2(e)). The EXAFS fitting curves and corresponding structural parameters for Fe_1/SCN-cm are shown in Fig. 2(f) and Table S3 in the ESM. The coordination numbers of Fe–N and Fe–S bonds are around 4 and 1, respectively. Compared with the intensity maximum at 5.5–8 $Å^{-1}$ raising from Fe–O and Fe–Fe bonds in Fe reference samples (Figs. 2(g), 2(h), and 2(j)), the only maximum at approximately 5 $Å^{-1}$, assigned to the Fe–N bond, is detected in Fe_1/SCN-cm (Fig. 2(i)). These results further demonstrate that Fe only exists as single atomic forms in Fe_1/SCN-cm.

To certify the generality of the synthetic strategy, Zn, Cr, and Mn single atoms anchored on SC were synthesized. PXRD patterns (Fig. 3(a)), SEM images (Fig. S14 in the ESM) show the layered graphitic structure of Zn_1/SCN-cm, Cr_1/SCN-cm, and Mn_1/SCN-cm. STEM images and the corresponding EDS mapping indicate the even distribution of Zn, Cr, and Mn in both samples (Figs. 3(b)–3(d)). XANES spectra and FT-EXAFS analysis confirmed that all metal (M) atoms in the catalysts exhibited M–N_x coordination, demonstrating that Mn, Zn, and Cr sites were atomically dispersed in M_1/SCN-cm (Fig. S15 in the ESM). These results suggest that this strategy can be used to synthesize several varieties of SACs.

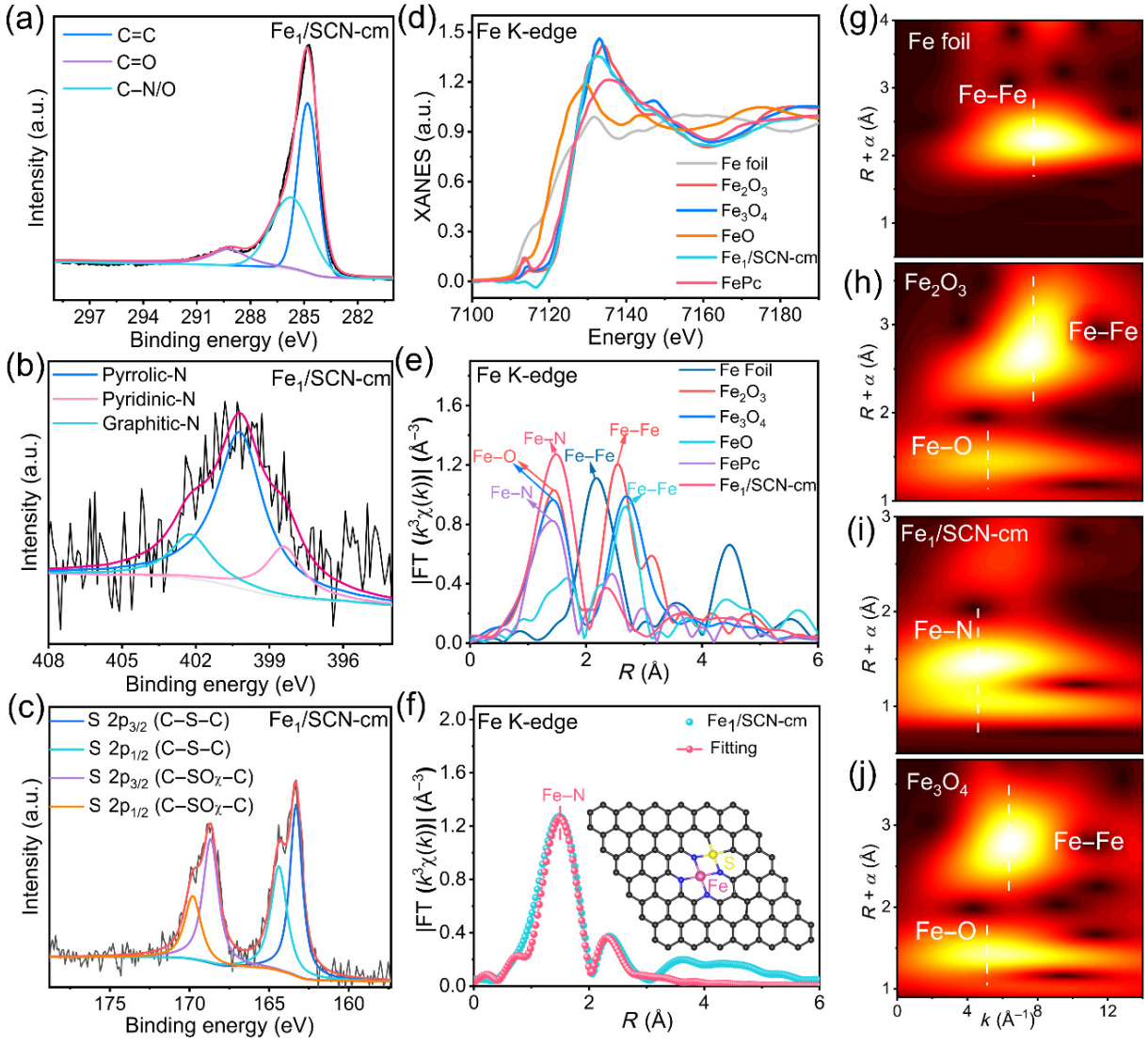

Figure 2 (a) C 1s, (b) N 1s, and (c) S 2p XPS spectra of Fe_1/SCN-cm. (d) Fe K-edge XANES and (e) FT-EXAFS spectra of Fe_1/SCN-cm with reference samples. (f) The corresponding EXAFS *R*-space fitting curves of Fe_1/SCN-cm. ((g)–(j)) Wavelet transform (WT) contour plots of Fe_1/SCN-cm with reference samples

The sulfur-doped Fe single atom catalysts with high surface area may be an excellent catalyst for ORR, and the properties of Fe_1/SCN-cm with reference samples were assessed by the three-electrode with a rotating disk electrode (RDE). Linear sweep voltammetry (LSV) curves are shown in Fig. 4(a). Fe_1/SCN-cm exhibit the highest catalytic properties with a half-wave potential ($E_{1/2}$) and onset potential (E_{onset}) of 0.92 and 1.00 V, respectively, outperforming commercial Pt/C catalyst (0.87 and 0.99 V) (Fig. 4(b)) and the untreated with KOH of Fe_1/SCN-cm (S_{BET} = 45.9 $m^2 \cdot g^{-1}$, 0.708 and 0.83 V) (Fig. S16 in the ESM). Balanced with the Fe loading and the content of defects, Fe_1/SCN-cm exhibits the highest ORR catalytic performance with the $E_{1/2}$ superior to other Fe_1/SCN-cm-*x* catalysts (*x* = 2, 4, 8, and 10 mg) (Fig. S17 in the ESM). Furthermore, ORR performance evaluation revealed that Zn_1/SCN-cm, Cr_1/SCN-cm, and Mn_1/SCN-cm exhibited $E_{1/2}$ of 0.791, 0.806, and 0.854 V, respectively (Fig. S18 in the ESM), with their diffusion-limited current densities all lower than that of Fe_1/SCN-cm. SC, the support, only performs negligible activity in this reaction, indicating Fe single atom is the main active site in Fe_1/SCN-cm. The results of SCN^- poisoning experiments further confirmed that Fe–N_x is the active site for ORR catalyzed by Fe_1/SCN-cm (Fig. S19 in the ESM). Moreover, Fe_1/SCN-cm shows the superiority among the most reported Fe-based SACs (Table S4 in the ESM), and Fe-doped on XC-72, synthesized via similar synthetic procedure almost inactive in ORR, indicating that canola meal-derived support presents excellent potential in fabricating highly efficient SACs.

More importantly, Fe_1/SCN-cm exhibits high stability in ORR with only 13 mV decrease in $E_{1/2}$ after 10,000 cycles of cyclic voltammograms (CVs) (Fig. 4(c)), while commercial Pt/C shows a 33 mV decline after 10,000 cycles of CVs (Fig. 4(d)). The positive correlation between the electrochemically active surface area (ECSA) and double-layer capacitance (C_{dl}) is shown in Figs. S20 and S21 in the ESM. The C_{dl} value of Fe_1/SCN-cm was calculated to be 23.35 $mF \cdot cm^{-2}$. The high C_{dl} value of Fe_1/SCN-cm indicated the enrichment of abundant Fe active sites on the carbon matrix, thereby endowing it with a higher ECSA (Figs. S20 and S21 in the ESM). To further reveal electron transfer number as well as the corresponding reaction mechanism in Fe_1/SCN-cm involved ORR catalytic system, the LSV curves with different rotating speeds were

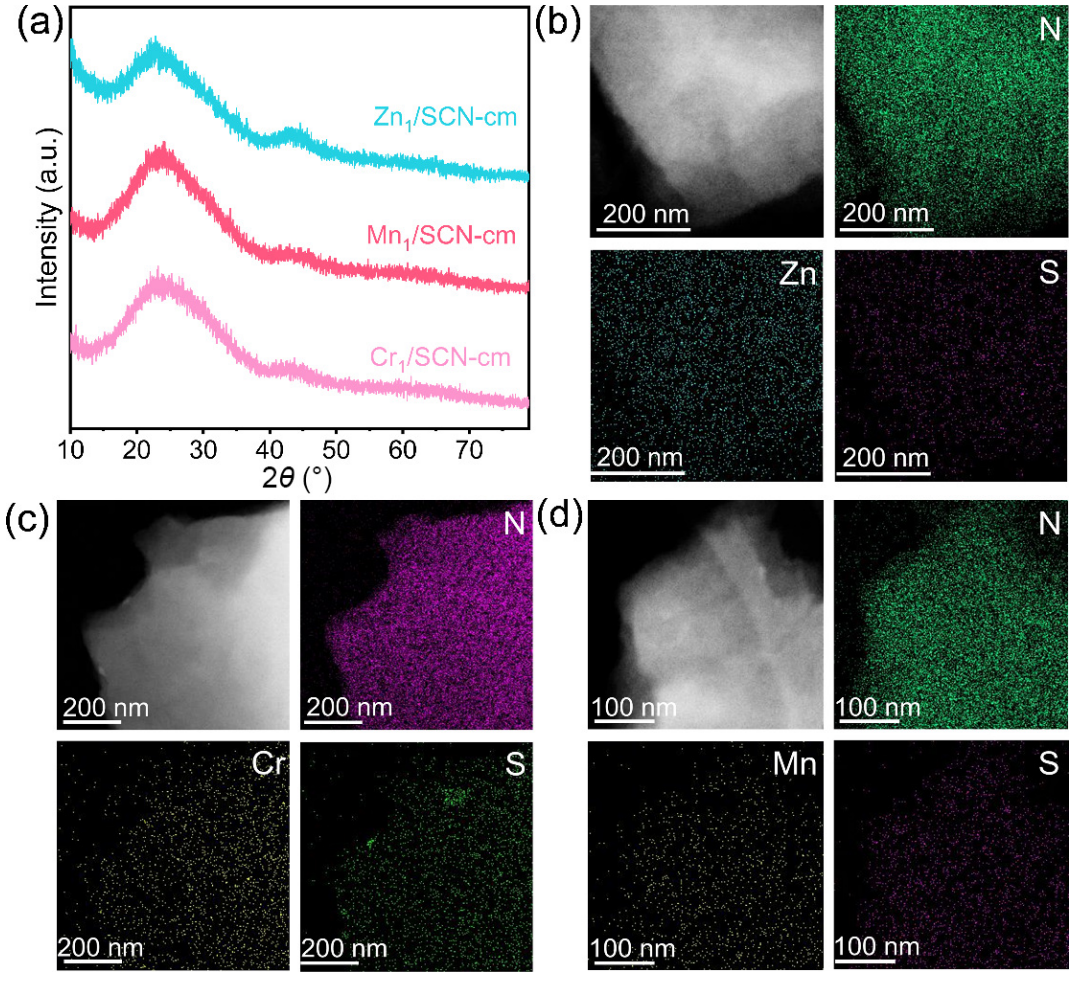

Figure 3 (a) XRD patterns of Cr_1/SCN-cm, Mn_1/SCN-cm, and Zn_1/SCN-cm. ((b)–(d)) STEM images and the corresponding EDS mapping images of (b) Zn_1/SCN-cm, (c) Cr_1/SCN-cm, and (d) Mn_1/SCN-cm.

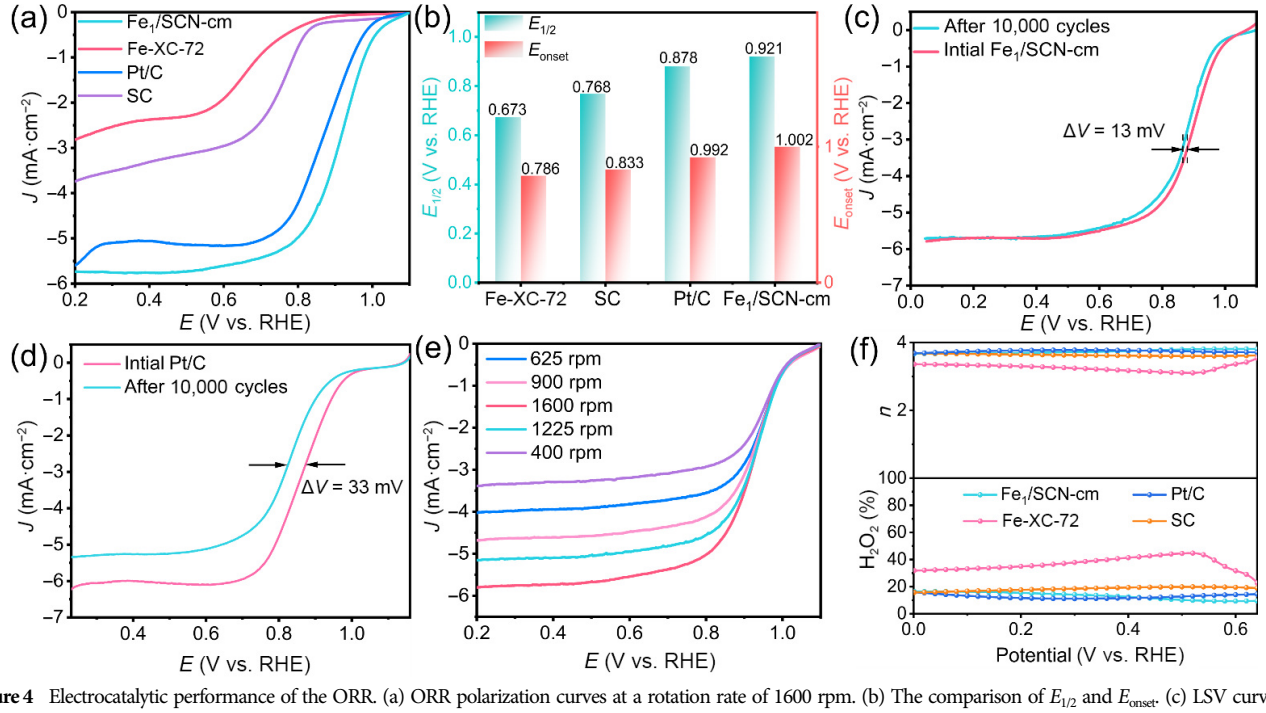

Figure 4 Electrocatalytic performance of the ORR. (a) ORR polarization curves at a rotation rate of 1600 rpm. (b) The comparison of $E_{1/2}$ and E_{onset}. (c) LSV curves of Fe_1/SCN-cm before and after 10,000 cycles in 0.1 M KOH. (d) LSV curves of Pt/C before and after 10,000 cycles in 0.1 M KOH. (e) The ORR polarization curves at different rotating rates of Fe_1/SCN-cm. (f) Electron-transfer number (n) (top) and H_2O_2 yield (bottom) vs. potential.

performed (Fig. 4(e)). Due to the accelerated diffusion, the current density was linearly enlarged with increasing the rotating speed, with the calculated electron transfer number ranging from 3.98 to 4.51, suggesting a 4 e ORR pathway (Fig. S22 in the ESM). The hydrogen peroxide production rate of 9.4% is detected in the Fe_1/SCN-cm involved catalytic system with the calculated electron transfer number of 3.98, which is similar to that in Pt/C involved catalytic system (Fig. 4(f)). These results further validate that Fe_1/SCN-cm can catalyze ORR via a 4e reaction mechanism. The Tafel slopes were calculated to determine the kinetics in this reaction. Fe_1/SCN-cm shows the lowest Tafel slope of 106.7 mV·dec^{-1}, compared with that of Pt/CN (106.9 mV·dec^{-1}), indicating a faster kinetics of Fe_1/SCN-cm (Fig. S23 in the ESM). Moreover, the kinetics of Fe_1/SCN-cm can also be improved when adding conductive graphite (XC-72) into the ink (84.7 mV·dec^{-1}). The high ORR catalytic performance of Fe_1/SCN-cm illustrates that the sulfur content as well as the layered structure of canola meal in canola meal makes it suitable for fabricating single atom catalysts.

Based on its exceptional ORR activity, the air cathode of a quasi-solid-state ZABs was assembled using Fe_1/SCN-cm as the catalyst to validate its practical application value. The experimental setup comprised a zinc foil, alkaline electrolyte, and a triphasic air cathode integrated with the Fe_1/SCN-cm or Pt/C catalyst-coated gas diffusion layer (Fig. 5(a)). Fe_1/SCN-cm-based ZABs exhibited an open-circuit voltage (OCV) of 1.48 V, surpassing that of the commercial Pt/C catalyst (1.42 V) (Fig. 5(b)). The peak power density of the Fe_1/SCN-cm-based ZABs reached 160.2 mW·cm^{-2}, significantly exceeding 114.8 mW·cm^{-2} achieved by the Pt/C-based ZABs (Fig. 5(c)). Galvanostatic discharge testing at a current density of 10 mA·cm^{-2} revealed that the specific capacity of 789.8 mAh·g_{Zn}^{-1} for the Fe_1/SCN-cm-based ZAB, superior to the 748.4 mAh·g_{Zn}^{-1} of the commercial Pt/C-based ZABs (Fig. 5(d)). Discharge tests at various current densities consistently showed higher voltage plateaus for the Fe_1/SCN-cm-based ZABs compared to the Pt/C-based counterpart (Fig. 5(e)). Following discharge testing, the Fe_1/SCN-cm-based ZABs effectively recovered to their initial voltage plateau, demonstrating excellent rate capability and electrochemical reversibility. Furthermore, during galvanostatic cycling stability tests, Fe_1/SCN-cm + RuO_2-based ZABs maintained stable voltage plateaus with minimal fading after 320 h of continuous operation at 10 mA·cm^{-2}. In stark contrast, Pt/C + RuO_2-based ZABs exhibited significant voltage decay and performance degradation after only 122 h (Fig. 5(f)). These results collectively indicate the outstanding potential of the Fe_1/SCN-cm catalyst as a cathode material for practical device applications.

3 Conclusions

In conclusion, Fe_1/SCN-cm was fabricated via impregnating Fe on canola meal-derived S, N co-doped carbon catalysts. Fe_1/SCN-cm exhibits high catalytic activity ($E_{1/2}$ and E_{onset} of 0.92 and 1.002 V), and stability (13 mV decreases after 10,000 cycles) in ORR. The experimental results illustrate that the layer porous structure induced by molten K^+ and the sulphur-derived from canola meal results in the high ORR catalytic activity of Fe_1/SCN-cm. Moreover, Fe_1/SCN-cm-based ZABs show a high OCV with 1.48 V and a cyclability (nearly unchanged after 320 cycles), suggesting their high potential in practical applications.

Electronic Supplementary Material: Supplementary material (detailed experimental procedures, materials synthesis, additional ORR catalytic performance data, XRD patterns, SEM/STEM images, N_2 adsorption–desorption isotherms, XPS spectras, XANES spectroscopy, other supplementary figures, and tables) is available in the online version of this article at https://doi.org/10.26599/NR.2025.94908051.

Data availability

All data needed to support the conclusions in the paper are

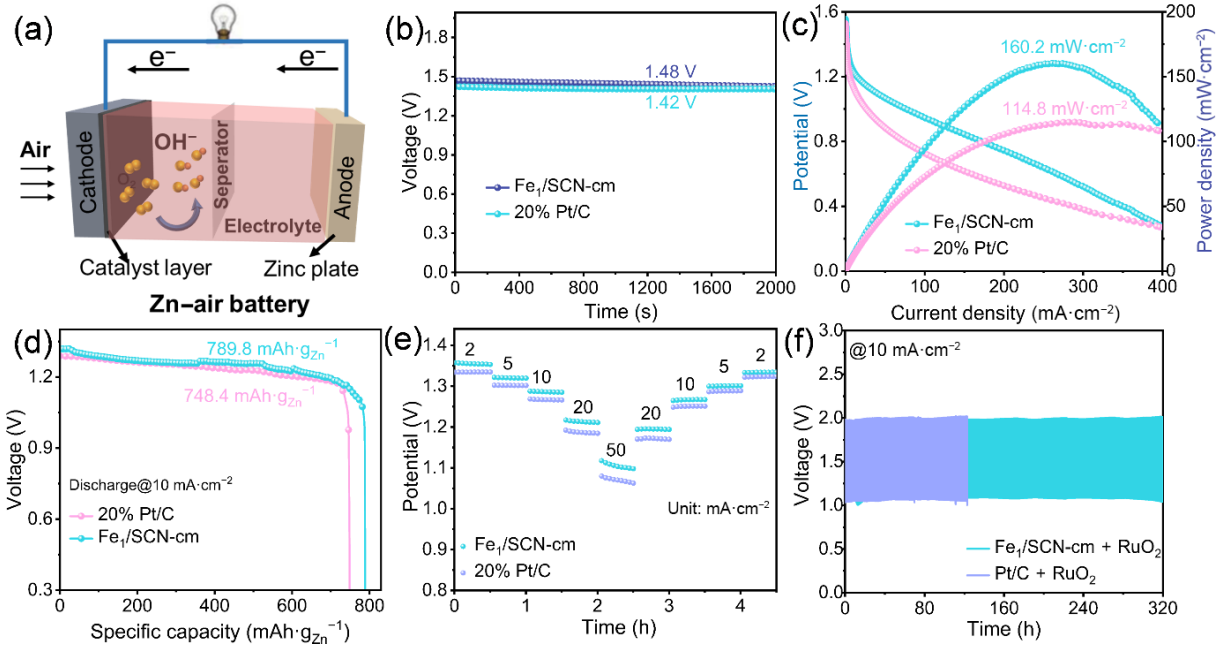

Figure 5 (a) Schematic diagram of the assembled quasi-solid-state ZABs. (b) Open-circuit voltage curves. (c) Polarization curves and power density curves of ZABs based on Fe_1/SCN-cm and Pt/C. (d) Specific capacities of the ZABs at 10 mA·cm^{-2}. (e) Galvanostatic discharge curves at different discharge current densities. (f) Cycling test of the quasi-solid-state ZABs based on Fe_1/SCN-cm + RuO_2 or Pt/C + RuO_2 mixtures at 10 mA·cm^{-2}.

presented in the manuscript and the Electronic Supplementary Material. Additional data related to this paper may be requested from the corresponding author upon request.

Acknowledgements

We thank the Anhui Absorption Spectroscopy Analysis Instrument Co., Ltd. for XAFS measurements and analysis. This work was supported by Yuelushan Laboratory Seed Industry Special Program (No. YLS-2025-ZY04004) and Young Elite Scientists Sponsorship Program by CAST (No. 2022QNRC001).

Declaration of competing interest

All the contributing authors report no conflict of interests in this work.

Author contribution statement

Y. X.: Funding acquisition, project administration, supervision, and writing – review & editing. J. P. G.: Conceptualization, methodology, formal analysis, investigation, resources, data curation, writing – original draft, visualization. C. Y. H.: Data curation and writing – original draft. D. H. L.: Validation, data curation, formal analysis. B. L.: Supervision and formal analysis. T. H. W.: Verified the data accuracy. J. X. G.: Conceptualization. H. R. Z.: Analyzed the data. X. L.: Investigation. All the authors have approved the final manuscript.

Use of AI statement

None.

References

[1] Gan, T.; Wang, D. S. Atomically dispersed materials: Ideal catalysts in atomic era. *Nano Res.* **2024**, *17*, 18–38.

[2] Han, L. L.; Cheng, H.; Liu, W.; Li, H. Q.; Ou, P. F.; Lin, R. Q.; Wang, H. T.; Pao, C. W.; Head, A. R.; Wang, C. H. et al. A single-atom library for guided monometallic and concentration-complex multimetallic designs. *Nat. Mater.* **2022**, *21*, 681–688.

[3] Ji, S. F.; Chen, Y. J.; Wang, X. L.; Zhang, Z. D.; Wang, D. S.; Li, Y. D. Chemical synthesis of single atomic site catalysts. *Chem. Rev.* **2020**, *120*, 11900–11955.

[4] Liu, L. C.; Corma, A. Metal catalysts for heterogeneous catalysis: From single atoms to nanoclusters and nanoparticles. *Chem. Rev.* **2018**, *118*, 4981–5079.

[5] Zhang, L. L.; Zhou, M. X.; Wang, A. Q.; Zhang, T. Selective hydrogenation over supported metal catalysts: From nanoparticles to single atoms. *Chem. Rev.* **2020**, *120*, 683–733.

[6] Fang, J. J.; Hu, Q. Q.; Zhu, C. Y.; Mao, J. J. Chemical microenvironment regulation of single-atom catalysts in photocatalysis. *Chem. Commun.* **2025**, *61*, 7178–7200.

[7] Jiao, W. S.; Ren, Z. H.; Cui, Z. B.; Ma, C.; Shang, Z. A.; Chen, G. Z.; Lu, R. H.; Gan, T.; Wang, Z. Y.; Xiong, Y. et al. All-round enhancement induced by oxophilic single Ru and W atoms for alkaline hydrogen oxidation of tiny Pt nanoparticles. *Nat. Commun.* **2025**, *16*, 883.

[8] Ma, R. Z.; Zhang, J.; Gong, J. X.; Lin, Y. X.; Zhang, J. L.; Huang, Z. Q.; Chang, C. R.; Liu, S. J.; Zhu, W.; Wang, Y. X. et al. The cooperative effects of the Rh–M dual-metal atomic pairs in formic acid oxidation. *Angew. Chem., Int. Ed.* **2025**, *64*, e202503095.

[9] Xiong, Y.; Dong, J. C.; Huang, Z. Q.; Xin, P. Y.; Chen, W. X.; Wang, Y.; Li, Z.; Jin, Z.; Xing, W.; Zhuang, Z. B. et al. Single-atom Rh/N-doped carbon electrocatalyst for formic acid oxidation. *Nat. Nanotechnol.* **2020**, *15*, 390–397.

[10] Zhang, M. X.; Peng, J. H.; Zhang, Z.; Ma, X. J.; Xing, S. Z.; Liu, Y. W. Electron-deficient defect sites in polyoxometalate-based metal–organic frameworks induced by atom substitution-modulated host–guest interaction. *Sci. Bull.* **2025**, *70*, 1986–1993.

[11] Chang, J. W.; Zhang, Q.; Yu, J. K.; Jing, W.; Wang, S. Y.; Yin, G. C.; Waterhouse, G. I. N.; Lu, S. Y. A Fe single atom seed-mediated strategy toward Fe_3C/Fe–N–C catalysts with outstanding bifunctional ORR/OER activities. *Adv. Sci.* **2023**, *10*, 2301656.

[12] Ma, R. Z.; Li, Q. H.; Yan, J.; Tao, Y.; Hu, S. Y.; Liu, D. H.; Gong, J. X.; Xiong, Y. Thermodynamically controllable synthesis of ZIF-8 exposing different facets and their applications in single atom catalytic oxygen reduction reactions. *Nano Res.* **2023**, *16*, 9618–9624.

[13] Wang, X. C.; Kang, Z. W.; Wang, D.; Zhao, Y. F.; Xiang, X.; Shang, H. S.; Zhang, B. Electronic structure regulation of the Fe-based single-atom catalysts for oxygen electrocatalysis. *Nano Energy* **2024**, *121*, 109268.

[14] Zhao, Y. F.; Shen, Z. Y.; Huo, J. J.; Cao, X. J.; Ou, P. F.; Qu, J. P.; Nie, X. M.; Zhang, J. Q.; Wu, M. H.; Wang, G. X. et al. Epoxy-rich Fe single atom sites boost oxygen reduction electrocatalysis. *Angew. Chem., Int. Ed.* **2023**, *62*, e202308349.

[15] Zheng, H. R.; Wang, S. B.; Liu, S. J.; Wu, J.; Guan, J. P.; Li, Q.; Wang, Y. C.; Tao, Y.; Hu, S. Y.; Bai, Y. et al. The Heterointerface between Fe_1/NC and Selenides Boosts Reversible Oxygen Electrocatalysis. *Adv. Funct. Mater.* **2023**, *33*, 2300815.

[16] Zhang, L.; Meng, Q. L.; Zheng, R. X.; Wang, L. Q.; Xing, W.; Cai, W. W.; Xiao, M. L. Microenvironment regulation of M–N–C single-atom catalysts towards oxygen reduction reaction. *Nano Res.* **2023**, *16*, 4468–4487.

[17] Chen, Y.; Lin, J.; Pan, Q.; Liu, X.; Ma, T. Y.; Wang, X. D. Inter-metal interaction of dual-atom catalysts in heterogeneous catalysis. *Angew. Chem., Int. Ed.* **2023**, *62*, e202306469.

[18] Tang, T. M.; Bai, X.; Wang, Z. L.; Guan, J. Q. Structural engineering of atomic catalysts for electrocatalysis. *Chem. Sci.* **2024**, *15*, 5082–5112.

[19] Fan, L. L.; Wei, X. F.; Li, X. T.; Liu, Z. N.; Li, M. F.; Liu, S.; Kang, Z. X.; Dai, F. N.; Lu, X. Q.; Sun, D. F. Phosphorus-doped iron-nitrogen-carbon catalyst with penta-coordinated single atom sites for efficient oxygen reduction. *Nano Res.* **2023**, *16*, 1810–1819.

[20] Pei, Z. H.; Zhang, H. B.; Guo, Y.; Luan, D. Y.; Gu, X. J.; Lou, X. W. Atomically dispersed Fe sites regulated by adjacent single Co atoms anchored on N–P Co-doped carbon structures for highly efficient oxygen reduction reaction. *Adv. Mater.* **2024**, *36*, 2306047.

[21] Han, J. W.; Xu, Q.; Rong, J. X.; Zhao, X.; She, P.; Qin, J. S.; Rao, H. Molecular engineering of porous Fe–N–C catalyst with sulfur incorporation for boosting CO_2 reduction and Zn–CO_2 battery. *Adv. Sci.* **2024**, *11*, 2407063.

[22] Peng, C.; Wang, M. Y.; Li, S.; Zeng, X. Z.; Wang, J. Y.; Wang, W. H.; Zhang, Z. R.; Ye, M. F.; Wei, X. W.; Wu, K. L. et al. A general strategy based on hetero-charge coupling effect for constructing single-atom sites. *Angew. Chem., Int. Ed.* **2024**, *63*, e202408771.

[23] Zhang, S. Y.; Sun, B. W.; Liao, K.; Wang, X.; Chen, Z. Y.; Wang, J. J.; Hu, W. B.; Han, X. P. Boosting oxygen reduction reaction performance of Fe single-atom catalysts via precise control of the coordination environment. *Adv. Funct. Mater.* **2025**, *35*, 2425640.

[24] Wang, F. Q.; Zhang, R.; Zhang, Y. Y.; Li, Y.; Zhang, J.; Yuan, W. H.; Liu, H.; Wang, F.; Xin, H. L. Modulating electronic structure of atomically dispersed nickel sites through boron and nitrogen dual coordination boosts oxygen reduction. *Adv. Funct. Mater.* **2023**, *33*, 2213863.

[25] Yang, Y.; Wang, G.; Zhang, S. S.; Jiao, C.; Wu, X. Y.; Pan, C. B.; Mao, J. J.; Liu, Y. Boron in the second coordination sphere of Fe single atom boosts the oxygen reduction reaction. *ACS Appl. Mater. Interfaces* **2024**, *16*, 16224–16231.

[26] Wang, Z.; Xu, R. J.; Ye, Q. T.; Jin, X. Y.; Lu, Z.; Yang, Z. B.; Wang,

Y.; Yan, T.; Liu, Y. P.; Pan, Z. J. et al. Tailoring first coordination sphere of dual-metal atom sites boosts oxygen reduction and evolution activities. *Adv. Funct. Mater.* **2024**, *34*, 2315376.

[27] Sun, H.; Wang, M. F.; Du, X. C.; Jiao, Y.; Liu, S. S.; Qian, T.; Yan, Y. C.; Liu, C.; Liao, M.; Zhang, Q. H. et al. Modulating the d-band center of boron-doped single-atom sites to boost the oxygen reduction reaction. *J. Mater. Chem. A,* **2019**, *7*, 20952–20957.

[28] Liu, X.; Fang, J. J.; Guan, J. P.; Wang, S. B.; Xiong, Y.; Mao, J. J. Substance migration in the synthesis of single-atom catalysts. *Chem. Commun.* **2025**, *61*, 1800–1817.

[29] Zhao, C. X.; Liu, X. Y.; Liu, J. N.; Wang, J.; Wan, X.; Wang, C. D.; Li, X. Y.; Shui, J. L.; Song, L.; Peng, H. J. et al. Molecular recognition regulates coordination structure of single-atom sites. *Angew. Chem., Int. Ed.* **2023**, *62*, e202313028.

[30] Yu, L.; Li, Y. C.; Ruan, Y. F. Dynamic control of sacrificial bond transformation in the Fe–N–C single-atom catalyst for molecular oxygen reduction. *Angew. Chem., Int. Ed.* **2021**, *60*, 25296–25301.

[31] United States Department of Agriculture. Oilseeds: World markets and trade—Rising brazil biodiesel production hampers soybean oil exports [Online]. https://apps.fas.usda.gov/PSDOnline/CircularDownloader.ashx?year=2025&month=04&commodity=Oilseeds (accessed May 20, 2025).

[32] Sharma, S.; Lindquist, J. C.; Hwang, D. C. Canola/rapeseed as a potential source of alternative protein. *Food Rev. Int.* **2024**, *40*, 2306–2320.

[33] Tang, Y. R.; Ghosh, S. A review of the utilization of canola protein as an emulsifier in the development of food emulsions. *Molecules* **2023**, *28*, 8086.

[34] Wang, C. C.; Wu, J. P.; Bernard, G. M. Preparation and characterization of canola protein isolate-poly(glycidyl methacrylate) conjugates: A bio-based adhesive. *Ind. Crops Prod.* **2014**, *57*, 124–131.

[35] Hussain, S. M.; Bano, A. A.; Ali, S.; Rizwan, M.; Adrees, M.; Zahoor, A. F.; Sarker, P. K.; Hussain, M.; Arsalan, M. Z. U. H.; Yong, J. W. H. et al. Substitution of fishmeal: Highlights of potential plant protein sources for aquaculture sustainability. *Heliyon* **2024**, *10*, e26573.

[36] Li, R. Z.; Wang, D. S. Superiority of dual-atom catalysts in electrocatalysis: One step further than single-atom catalysts. *Adv. Energy Mater.* **2022**, *12*, 2103564.

[37] Liu, J. J.; Yang, J. R.; Dou, Y. H.; Liu, X. W.; Chen, S. H.; Wang, D. S. Deactivation mechanism and mitigation strategies of single-atom site electrocatalysts. *Adv. Mater.* **2025**, *37*, 202420383.

[38] Zhao, T. Y.; Wang, J. J.; Wei, Y. R.; Zhuang, Z. C.; Dou, Y. H.; Yang, J. R.; Li, W. H.; Wang, D. S. From lab-scale to industrialization: Atomically M–N–C catalysts for the oxygen reduction reaction. *Energy Environ. Sci.* **2025**, *18*, 3462–3501.

[39] Chen, Y. J.; Gao, R.; Ji, S. F.; Li, H. J.; Tang, K.; Jiang, P.; Hu, H. B.; Zhang, Z. D.; Hao, H. G.; Qu, Q. Y. et al. Atomic-level modulation of electronic density at cobalt single-atom sites derived from metal–organic frameworks: Enhanced oxygen reduction performance. *Angew. Chem., Int. Ed.* **2021**, *60*, 3212–3221.

[40] Zhang, E. H.; Tao, L.; An, J. K.; Zhang, J. W.; Meng, L. Z.; Zheng, X. B.; Wang, Y.; Li, N.; Du, S. X.; Zhang, J. T. et al. Engineering the local atomic environments of indium single-atom catalysts for efficient electrochemical production of hydrogen peroxide. *Angew. Chem., Int. Ed.* **2022**, *61*, e202117347.

[41] Han, A. L.; Wang, X. J.; Tang, K.; Zhang, Z. D.; Ye, C. L.; Kong, K. J.; Hu, H. B.; Zheng, L. R.; Jiang, P.; Zhao, C. X. et al. An adjacent atomic platinum site enables single-atom iron with high oxygen reduction reaction performance. *Angew. Chem., Int. Ed.* **2021**, *60*, 19262–19271.

[42] Zhang, H. W.; Chen, H. C.; Feizpoor, S.; Li, L. F.; Zhang, X.; Xu, X. F.; Zhuang, Z. C.; Li, Z. S.; Hu, W. Y.; Snyders, R. et al. Tailoring oxygen reduction reaction kinetics of Fe–N–C catalyst via spin manipulation for efficient zinc–air batteries. *Adv. Mater.* **2024**, *36*, 2400523.

[43] Han, A. L.; Sun, W. M.; Wan, X.; Cai, D. D.; Wang, X. J.; Li, F.; Shui, J. L.; Wang, D. S. Construction of Co_4 atomic clusters to enable Fe–N_4 motifs with highly active and durable oxygen reduction performance. *Angew. Chem., Int. Ed.* **2023**, *62*, e202303185.

[44] Zhuang, Z. C.; Li, Y.; Li, Y. H.; Huang, J. Z.; Wei, B.; Sun, R.; Ren, Y. J.; Ding, J.; Zhu, J. X.; Lang, Z. Q. et al. Atomically dispersed nonmagnetic electron traps improve oxygen reduction activity of perovskite oxides. *Energy Environ. Sci.* **2021**, *14*, 1016–1028.

[45] Chen, S. Y.; Li, X. Q.; Kao, C. W.; Luo, T.; Chen, K. J.; Fu, J. W.; Ma, C.; Li, H. M.; Li, M.; Chan, T. S.; et al. Unveiling the proton-feeding effect in sulfur-doped Fe–N–C single-atom catalyst for enhanced CO_2 electroreduction. *Angew. Chem., Int. Ed.* **2022**, *61*, e202206233.

[46] Zhang, J. T.; Zhang, M.; Zeng, Y.; Chen, J. S.; Qiu, L. X.; Zhou, H.; Sun, C. J.; Yu, Y.; Zhu, C. Z.; Zhu, Z. H. Single Fe atom on hierarchically porous S, N-codoped nanocarbon derived from porphyra enable boosted oxygen catalysis for rechargeable Zn–air batteries. *Small* **2019**, *15*, 1900307.